

A Universal Microscopic Patterned Doping Method for Perovskite Enables Ultrafast, Self-Powered, Ultrasmall Perovskite Photodiodes

Jiangong Cheng, Yang Ma, Wencai Zhou, Tong Zhang, Wenling Li, Xiaobo Zhang, Hui Yan, Jinpeng Li, Zilong Zheng,* Xiaoqing Chen,* and Yongzhe Zhang*

Novel metal halide perovskite is proven to be a promising optoelectronic material. However, fabricating microscopic perovskite devices is still challenging because the perovskite is soluble with the photoresist, which conflicts with conventional microfabrication technology. The size of presently reported perovskite devices is about 50 μm . Limited by the large size of perovskite optoelectronic devices, they cannot be readily adopted in the fields of imaging, display, etc. Herein a universal microscopic patterned doping method is proposed, which can realize microscale perovskite devices. Rather than by the conventional doping method, in this study the local Fermi level of perovskite is modulated by the redistributing intrinsic ion defects via a polling voltage. A satisfactorily stable polarized ion distribution can be achieved by optimization of the perovskite material and polling voltage, resulting in ultrafast (40 μs), self-powered microscale (2 μm) photodiodes. This work sheds light on a route to fabricate integrated perovskite optoelectronic chips.

1. Introduction

The metal halide perovskite is an ideal material for photoelectronic devices considering the excellent optoelectronic properties, for instance, wide optical absorption spectrum (300–800 nm)^[1–4] excellent optical absorption coefficient (10^5 cm^{-1}),^[5] long carrier diffusion length (1 μm),^[6] and high mobility ($100 \text{ cm}^2 \text{ V}^{-1} \text{ s}^{-1}$).^[6,7] The perovskite photoelectronic devices have successfully been applied in photodetection and light emitting, and recently extended to light-based logic devices or optical artificial synapse.^[8–11] Moreover, if the device size could be reduced to micrometer scale, the function of perovskite photoelectronic devices could be even broadened, for instance, imaging, displaying, optical chipset, and retinomorphic neural networks.

Unfortunately, most perovskite devices (except for simple perovskite resistors) could not be feasibly reduced to microscale,

considering the limitation of the junction width and the resolution of the electrode pattern. The microscopic patterned doping has been the bottleneck problem for realizing various microscopic perovskite photoelectronic devices, because perovskite is soluble to photoresist and, therefore, incompatible with conventional microscopic doping methods based on photolithography. For example, when adopting vertical sandwiched configuration, the device size is limited by the resolution of thermally deposited electrode pattern which is $\approx 50 \mu\text{m}$ (determined by the resolution of shadow mask).^[12] Instead, when using in-plane configuration (where the electrode pattern resolution is not a problem if it is prepared prior to the deposition of perovskite film), the width of the pn junction becomes the limiting factor because of the difficulty in microscale patterned doping that the perovskite is not compatible with the conventional photolithography-based doping due to its solubility in photoresist.^[13] In order to solve this problem, recent studies employed patterned external modifier materials to extrinsically dope the perovskite (C_{60} ,^[14] bathocuproine,^[15] and MoO_3 ^[16]) with heterojunction. Although this method can dope the perovskite without using photolithography, it introduces external materials, which result in deep level defects at the interface and the other potential technical problems.

J. Cheng, W. Zhou, T. Zhang, W. Li, H. Yan, Z. Zheng
College of Material Sciences and Engineering
Beijing University of Technology
Beijing 100124, China
E-mail: zilong.zheng@bjut.edu.cn

Y. Ma, X. Chen, Y. Zhang
Key Laboratory of Optoelectronics Technology
College of Microelectronics
Faculty of Information Technology
Beijing University of Technology
Beijing 100124, China
E-mail: chenxiaoqing@bjut.edu.cn; yzzhang@bjut.edu.cn

X. Zhang
School of Physics and Engineering
Henan University of Science and Technology
263 Kaiyuan Avenue, Luoyang 471003, China

J. Li
Key Laboratory of Luminescence and Optical Information
Ministry of Education
School of Physical Science and Engineering
Beijing Jiaotong University
Beijing 100044, China

The ORCID identification number(s) for the author(s) of this article can be found under <https://doi.org/10.1002/adma.202300691>

DOI: 10.1002/adma.202300691

The recently revealed self-doping phenomenon sheds light on developing a universal patterned microscopic doping method. The ionic defects in the perovskite lattice can modulate the local doping level.^[17] As long as they are dissociated from the lattice sites under external bias and form Frenkel defects (mobile interstitial ions and ion vacancies), they could function as shallow dopants to tune the Fermi level.^[17–25] This self-doping phenomenon can be employed in microscale patterned doping of perovskite to either p-, i-, or n-type perovskite.

Based on these recent findings, a universal patterned microscale doping strategy becomes possible by using patterned electrodes with proper polling voltage (V_{poll}) treatment, in order to avoid photoresist solution.^[5, 26–28] To confirm this strategy, in this work, we attempted to fabricate a microscale pn junction via a self-doping phenomenon. We chose pn junction to demonstrate a universal patterned microscale doping strategy, because it is the element unit for diodes and many other photoelectronic devices. One may suspect whether the ions could relax to original positions reversely after removing V_{poll} . Fortunately, our results show that, as long as the ion migration is properly adjusted, the redistributed ions could hold their positions and their final distribution could be satisfactorily stable for 36 h. Based on this approach, a microscale pn junction photodetector with a 2 μm length was fabricated, which is an ideal pixel device of a large and dense image sensor. Moreover, it exhibited a satisfactory photodetector performance (responsivity = 28.6 mA W^{-1} , special detectivity = 2.77×10^{11} Jones, response time = 35 μs , and bandwidth = 11.3 kHz). Therefore, we solved the bottleneck problem by the self-doping phenomenon of perovskite so as the photoresist is no longer avoided. This advance may reveal possible routes for microscopic transistors, complementary metal–oxide–semiconductor (CMOS), and other devices.

2. Results and Discussion

A pair of indium-tin oxide (ITO) stripe electrodes with 2 μm distance was fabricated on precleaned glass by photolithography and dry etching. The perovskite film was then prepared on the upper side of the ITO glass so that a lateral microscale device (ITO/Perovskite (2 μm)/ITO) was completed (control device). The device structure and its optical microscope image are shown in **Figure 1a**, where the red dashed rectangle is the gap area (2 $\mu\text{m} \times 80 \mu\text{m}$) and the red spot is the laser spot. Due to its symmetric structure, the device shows symmetric I – V characteristics from -2.5 to $+2.5$ V as indicated by the black curve in **Figure 1b**, indicating that the as-prepared perovskite film was symmetrically doped. Under either positive or negative bias, the device shows nonlinear increasing I – V curve. The nonlinear I – V characteristics indicate that the ITO/perovskite interfaces are Schottky contact rather than Ohmic contact, as shown in **Figure 1c**. Our further analysis in **Figure S1** (Supporting Information) shows that the two Schottky diodes could be modeled as Zener diodes.

In order to realize a microscale perovskite pn homojunction, a polling voltage (+3 V) was applied across the electrodes for 300 s. As expected, the I – V curve shows obvious rectification character as indicated by the red curve in **Figure 1b**, suggesting the successful formation of a homojunction. The maximum rectification ratio (defined as the ratio of current values under $+2.5$

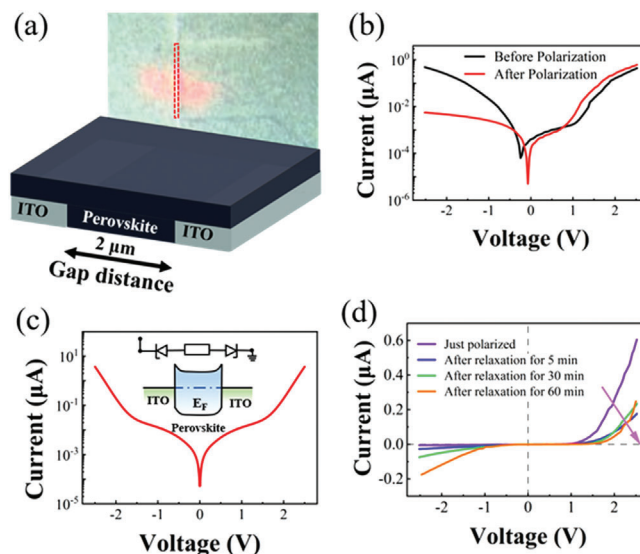


Figure 1. a) Lateral structure of ITO/perovskite/ITO. b) I – V curve of unpolarized and control device. c) Band alignment of pristine ITO/perovskite/ITO device and equivalent circuit. d) I – V curve with different relaxation times of the control device.

and -2.5 V) of the device is 110. However, the polarized ion distribution could not conserve after 60 min relaxation, as indicated by the time-dependent relaxation profile shown in **Figure 1d**, because the ions tend to reversely migrate to their original positions. The perovskite composition should be optimized to improve the rectification ratio and the stability.

In order to solve this problem, we attempted to increase the ion migration activation energy through optimizing the perovskite composition, so that the redistributed ions would hold their positions when the working voltage is not large. Namely, we finetune the ion migration property to enable a working window, which allows for both feasible redistributing the ions under higher V_{poll} and stable holding the distribution under lower working voltage. In order to prolong the relaxation process, we need to slow down (but not prevent) the ion migration to realize controllable and stabilized ion distribution, which consequently enables a practical working window. Our method is to blend the 3D perovskite film with 2D perovskite, which is reported to be able to inhibit the ion migration.^[29–31] As reported, blending the precursor solution with phenylethylammonium iodide (PEAI) or guanidine chloride (GuCl) could effectively form 3D/2D hybrid perovskite with suppressed ion migration.^[30] Therefore, in the subsequent experiments, PEAi or GuCl was added to the perovskite precursor solution. The devices treated with 20 mmol L^{-1} PEAi show longer relaxation time than those treated with GuCl (which relaxes within roughly 2 h, as shown in **Figure S2** in the Supporting Information), suggesting that the ion migration is sufficiently slow. This is further confirmed by our theoretical calculations. Our result shows that in pristine perovskite, GuCl-doped perovskite, and PEAi-doped perovskite, the activation energies of the most mobile ionic defect (V_i) are 0.38, 0.41, and 0.89 eV, respectively. Namely, the introduction of PEAi is more effective than GuCl in inhibiting the process of ion migration (**Figure 2d**).

Similar to the control device, the device still shows symmetrical I – V characteristics before applying V_{poll} and rectifying I – V

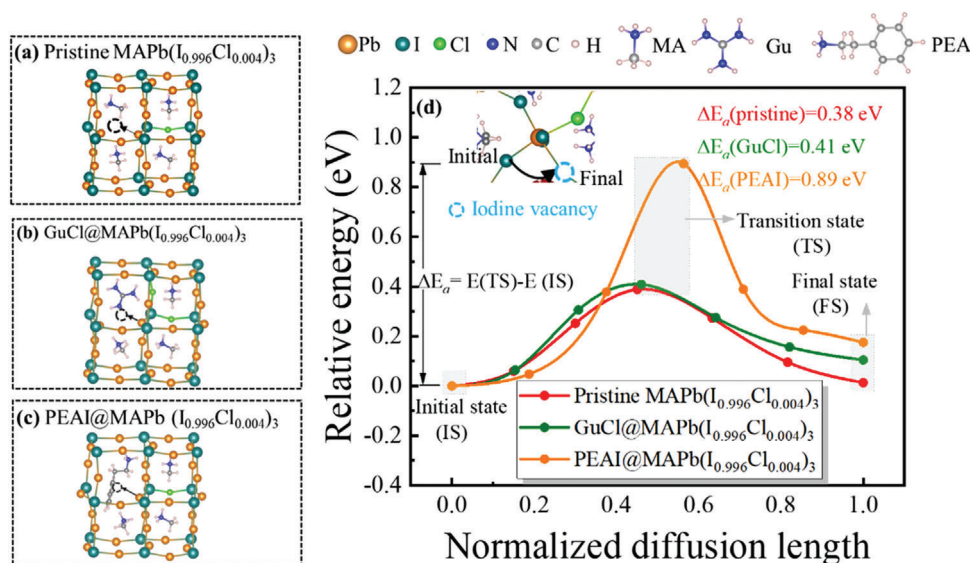


Figure 2. a–c) Schematic diagram of the pristine perovskite structure (a) and the structure after doping with GuCl (b) and PEAI (c). d) Activation energy diagram of ion migration before and after doping.

after applying V_{poll} , as shown in **Figure 3a**. Thanks to the suppressed ion migration, the relaxation process is prolonged to above 36 h, as shown in **Figure 3b**. In addition, the rectifying ratio is significantly improved from 110 to 4.1×10^3 after applying $V_{\text{poll}} = 3$ V for 300 s. The dark saturation current of the diode is 0.46 nA, suggesting ideal diode performance.

After obtaining a stable diode, we further characterized its performance as a photodetector to evaluate its potential as an imaging sensor pixel. We first characterized the responsivity (R) and specific detectivity rate (D^*) of our photodetectors, which are defined in Equations (1) and (2)

$$R = \frac{I_{\text{ph}}}{P_{\text{in}}} \quad (1)$$

$$D^* = R \sqrt{\frac{A}{2qI_d}} \quad (2)$$

where I_{ph} is the net photocurrent, P_{in} is the illumination power of the laser, A is the effective active area, q is the elementary charge, and I_d is the dark current, respectively.

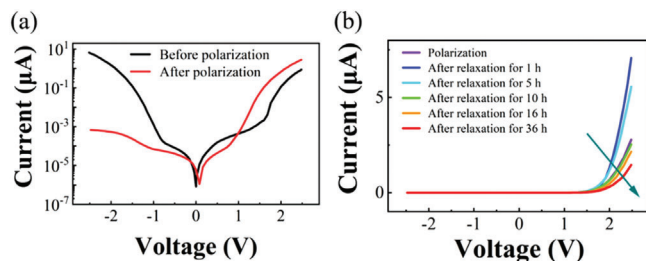


Figure 3. a) I – V curves before and after polarization. b) Dependence of I – V curve of PEAI-treated device on relaxation time.

The extracted responsivity and specific detectivity are 28.6 mA W^{-1} and $2.77 \times 10^{11} \text{ Jones}$, respectively. In addition, we characterized the rising and the falling time (defined as the time from 10% to 90% of the maximum photocurrent, or vice versa), since the response time is one of the advantages of photodiodes as image sensor pixels. As shown in **Figure 4a,b**, the device shows an ultra-fast response speed under 0 V bias; the rising and the falling time are 47.5 and 35.0 μs , respectively, under a 685 nm laser of 199 nW while the device bandwidth is 11.3 kHz, which is fast enough for a high-speed camera,^[32] as derived from the frequency-dependent response gain of the device. Compared with the control device, the detectivity of the PEAI-treated devices is increased by ten times (primarily due to the decreased dark current), and the response speed and frequency-dependent response gain are improved by one order of magnitude, as shown in **Figure S3** (Supporting Information). A comparison of the key parameters of the photodiode in this work with other reported photodiodes is shown in Table S2 (Supporting Information). The laser waveform is modulated to be a square wave while the response photocurrent of the device is amplified before being recorded by the

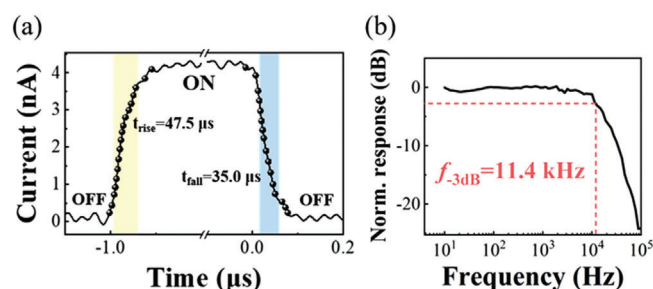


Figure 4. a) Time-resolved photocurrent for the polarized device under 0 V bias. b) Frequency-dependent performance of polarized device implying the bandwidth is 11.4 kHz.

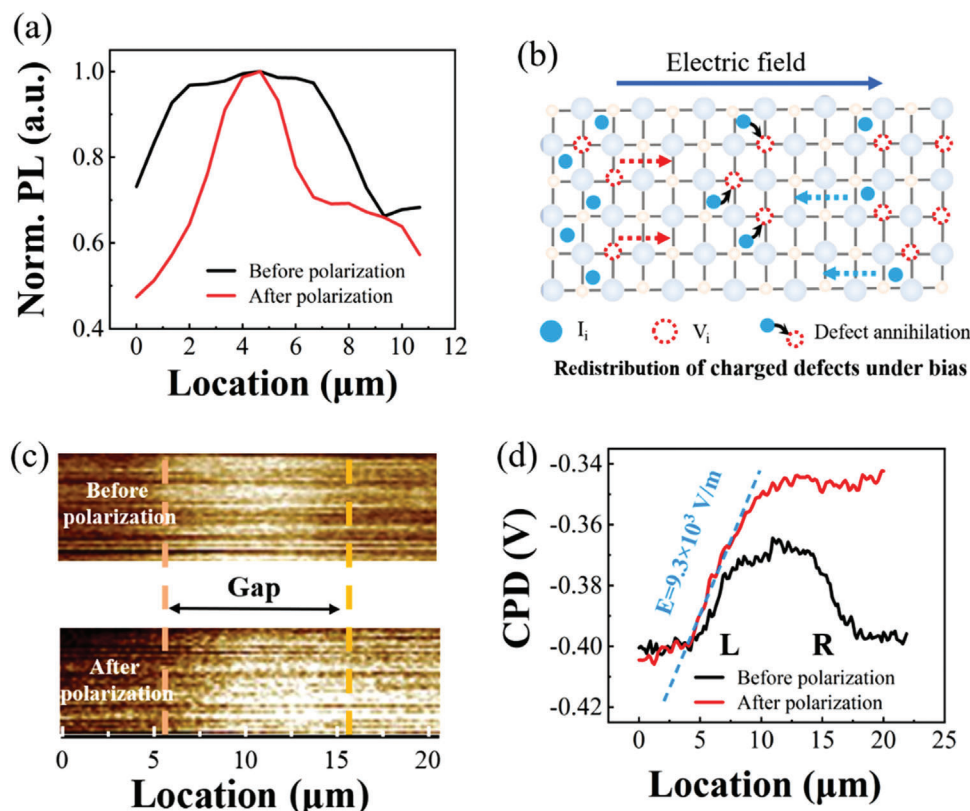


Figure 5. a) PL mapping profile across the device gap. b) Scheme of the migration of mobile ion defects under bias. c) Changes of surface potential of devices before and after polarization. d) 1D surface potential distribution extracted from (c).

oscilloscope. The experimental setup is shown in Figure S4 (Supporting Information).

After obtaining a device with stable rectifying characteristics, we are allowed to study the spatial profile of the device gap before and after polarization in detail. In order to map the spatial distribution of the relocated ions and the modulated energy diagram, we sequentially characterized the photoluminescence (PL) mapping (in which the relocated ions act as nonradiative recombination centers) and Kelvin probe force microscopy (KPFM). Note that in these experiments, we used devices with wider gaps (10 μm) due to the spatial resolution limit of the instruments. In the PL mapping experiment, the light spot size is about 0.3 μm. The measured PL profiles across the device gap before and after polarization are shown in Figure 5a. Before polarization, the PL intensity near the interfaces is about the same as in the gap center (in which the PL intensity ratio is 73%), indicating that the mobile ion concentration (which acts as nonradiative recombination centers) near the interfaces is about the same as in the gap center. Meanwhile, the PL intensity is slightly lower on both sides of the gap but higher in the middle. This is because the Schottky barrier will separate the photogenerated electrons and holes, leading to reduced radiative recombination of photogenerated carriers,^[33] while in the middle of the gap far from the Schottky barrier, most of the photogenerated carriers recombine with radiation. By contrast, after applying $V_{\text{poll}} = 5 \text{ V}$ for 300 s, the PL intensity near the interfaces reduced to only 47% relative to in the gap center, indicating that the mobile ion concentration near

the interfaces is obviously higher than the gap center. The abrupt difference between the PL intensities near the interface and in the gap is due to the accumulation of anions or cations on both sides of the Schottky barrier, resulting in a large number of vacancy or gap defects leading to nonradiative recombination.^[34,35] This result confirms the successful redistribution of the mobile ions by polarization treatment (most likely iodine interstitial I_i^- and iodine vacancy V_i^+),^[36] leading to the increase of nonradiative recombination on both sides of the gap. The schematic diagram of ion migration under bias is shown in Figure 5b. The directional migration of I_i^- and V_i^+ under bias voltage accumulates at the two interfaces, respectively, leading to an increase in the concentration of nonradiative composite defects at the interface, which results in a significant decrease in PL intensity at the interface. The ions' migration behavior is finally manifested by the decrease of PL strength at the interface.

The consequent effect of ion migration on the energy levels is then verified through the KPFM of the device gap before and after polarization, as shown in Figure 5c. The 1D contact potential difference (CPD) profiles across the gap before and after polarization are shown in Figure 5d. Before the polarization treatment, the CPD in the gap is symmetrically distributed. The low CPD on both sides of the gap and the high CPD in the middle are consistent with the expected two Schottky barrier models. By contrast, after applying $V_{\text{poll}} = 5 \text{ V}$ for 100 s, the left (L) side CPD in the gap is basically constant while the right (R) side CPD increases greatly. By comparing the device CPD profiles before and after

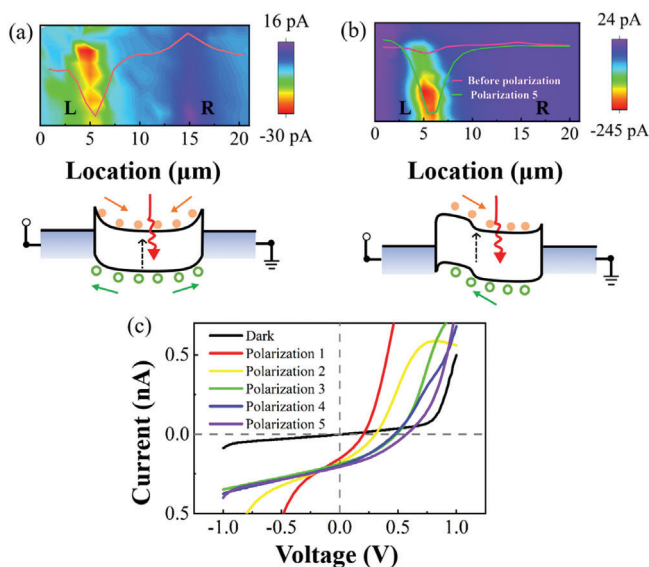


Figure 6. a) Photocurrent mapping of the device before polarization (wavelength = 685 nm, power = 7 nW) along with the red curve showing the position-dependent photocurrent. b) Photocurrent mapping of the device after five polarizations. c) The dependence of the device I–V curve under illumination on polarization treatment times showing that the open-circuit voltage and short-circuit current vary with polarization times.

polarization, we can observe that, after the device polarization, the band bending (corresponding to the electric field) increased while the junction area widened on the L side, but the band bending disappeared on the R side. This arises from the change of net doping, which is modulated by the ion migration. On the L side, the accumulation of mobile anions leads to p-type doping, while on the R side, the accumulation of cations leads to n-type doping, resulting in the formation of pn junction in the gap region, with an built-in electric field of $9.3 \times 10^3 \text{ V m}^{-1}$ which is calculated from the spatial gradient of the energy band.

Finally, the carrier dynamics under the polarized energy diagram is studied through mapping the device photocurrent under zero bias, as shown in **Figure 6a**. When the laser irradiates on the gap, the photogenerated carriers are generated. As shown in **Figure 6a**, before polarization treatment, the collected photocurrent is negative when illuminating the L side and positive when illuminating the R side, which confirms our proposed energy diagram above. In addition, the photocurrent is higher in the Schottky junction regions (either L or R) than in the gap, because the photogenerated carriers in the Schottky barrier junction region can be more efficiently separated by the electric field,^[37] than those in the flat-band region of the gap. Next, the device was subjected to small and large bias polarizations to study the relationship between the doping effect and the polarization voltage. When the device is polarized with a small bias voltage ($V_{\text{poll}} = 5 \text{ V}$ for 100 s), the overall effect is not obvious even after the device was polarized for four consecutive times (400 s) (**Figure S5**, Supporting Information). By contrast, when large voltage polarization is applied ($V_{\text{poll}} = 8 \text{ V}$ for 100 s), the photocurrent increased to 867.5% on the L side (from -22.76 to -197.81 pA) and reduced to 1.7% on the R side (from $+9.51$ to $+0.17 \text{ pA}$), as shown in **Figure 6b**. Namely, in our test condition, the polarization volt-

age amplitude must reach a threshold level to redistribute the ions.

In order to further verify the effect of ion directional migration on doping concentration, we measured the open-circuit voltage (V_{OC}) and short-circuit current (J_{SC}) variation of the devices with $2 \mu\text{m}$ gaps (wavelength = 685 nm, power = 7 nW) after a series of consecutive polarizations ($V_{\text{poll}} = 3 \text{ V}$ for 100 s), as shown in **Figure 6c**. In addition, through applying sequential polarization treatments, we observe that the V_{OC} noticeably increased from 0.21 to 0.58 V, while the J_{SC} slightly increased from 0.14 to 0.21 nA. The significant increment in V_{OC} suggests that the built-in electric potential is significantly increased due to the accumulation of the cations or anions at the corresponding sides.

The above explanation to the experimental results is verified through simulation by using the drift-diffusion program developed by Calado et al.^[38] According to the simulation results, before polarization, due to the built-in electric fields of the Schottky junctions (pointing from the perovskite to the ITO electrode), the ions are symmetrically distributed where the cations are attracted toward the electrodes and the anions are expelled from the electrodes, as shown by **Figure 7a**. The symmetric ion distribution results in symmetric energy diagram, as shown in **Figure 7c**. By contrast, after the polarization treatment of the device ($2 \mu\text{m}$) lasts for 100 s with a 3 V bias, as shown in **Figure 7b**, the anions and cations are accumulated near the L and R sides, respectively, which modulates the local Fermi levels toward p-doping and n-doping, respectively, resulting in a model pn junction, as shown in **Figure 7d**. Namely, the directional ion migration leads to self-doping of perovskite, resulting in the formation of pn homojunction in the device. The simulated rectifying characteristics of the device are shown in **Figure 7e**.

3. Conclusion

In order to realize microscopic perovskite optoelectronic devices, we developed a photoresist-free universal microscale patterned doping method based on the unique self-doping phenomenon of perovskite. In this approach, the intrinsic ion defects of perovskite were redistributed by applying an external electric field, which could modulate the microscale local doping level and the doping types (p, i, or n). In order to stabilize the redistributed ions, the material composition and applied polling voltages were optimized. Assisted with the optimized method, an ultrasmall photodiode with a $2 \mu\text{m}$ length was realized, which was the representative optoelectronic device. More importantly, the device showed an ideal device performance (dark saturation current is 5 nA, responsivity is 28.6 mA W^{-1} , specific detectivity is 2.77×10^{11} Jones, rise/fall times is 47.5/35.0 μs , and bandwidth is 11.4 kHz under 0 V bias), which confirmed the effectiveness of this method. In order to improve the photodetection properties, future study may focus on optimizing the perovskite bandgap, doping concentration, and crystallinity, which are beneficial for the responsivity, detectivity, and response speed. The microscopic patterned doping method proposed in this work is not only applicable to photodiode but also universally compatible to other perovskite devices. This method is able to break the size limit and will shed light on fabricating integrated perovskite optoelectronic chips.

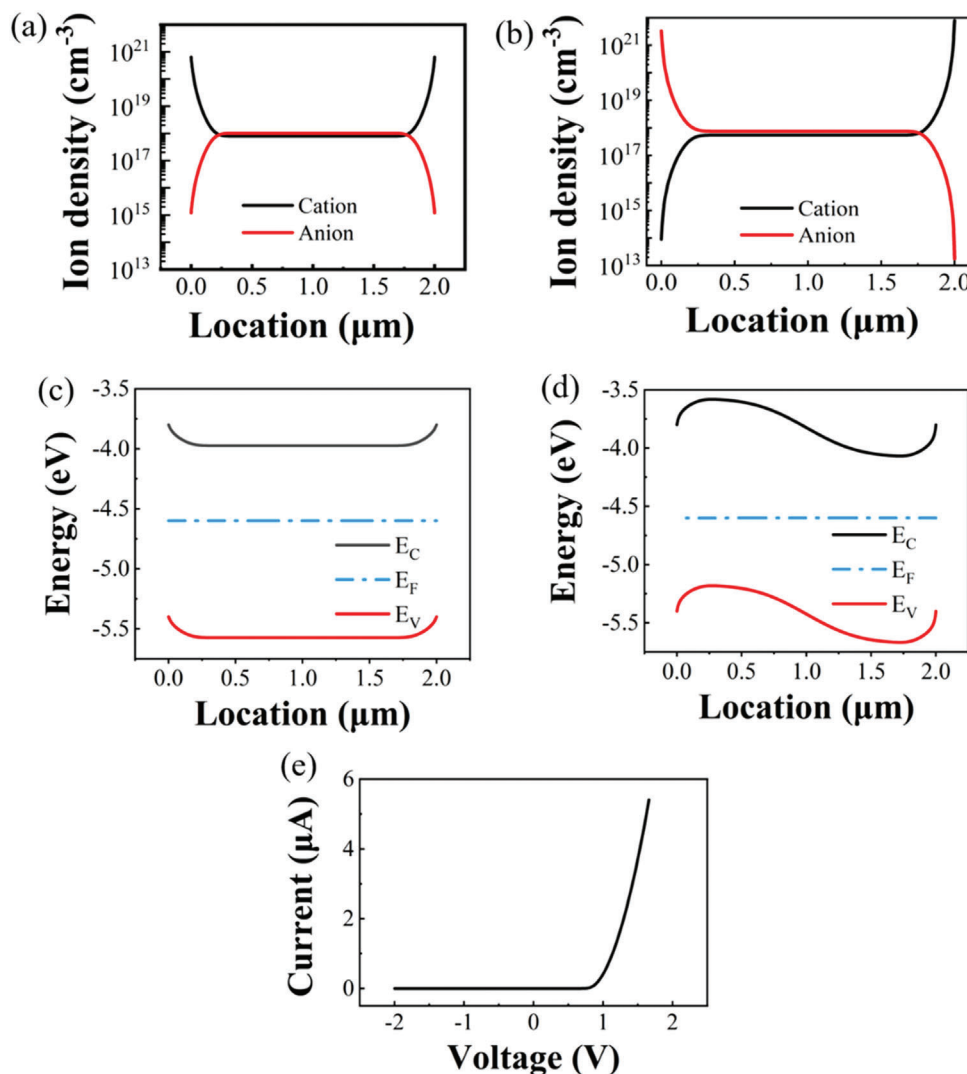


Figure 7. a,b) Simulated ion distribution before polarization (a) and after polarization (b). c) Simulation of energy level distribution of devices before polarization. d) Simulation of energy level distribution of devices after polarization. e) Simulation of I - V curve of polarized devices.

4. Experimental Section

Materials: Unless stated otherwise, all chemicals and solvents used as purchased without further purification, including GuCl (> 99.5%), PEAI (>99.5%), formamidine iodide (FAI, >99.5%), methylammonium iodide (MAI, >99.5%), and methylammonium chloride (MACl, >99.5%), from Xi'an Polymer Light Technology Corp. The solution including dimethyl sulfoxide (DMSO, 99.8%), *N,N*-dimethylformamide (DMF, 99.8%), and isopropanol (IPA, 99.5%) were obtained from Sigma-Aldrich.

Device Fabrication: The patterned ITO prepared via photoetching and ion etching as the substrate was precleaned using an ultrasonicator by deionized water, ethanol, acetone, ethanol, and deionized water, and subsequently irradiated by ultraviolet-ozone for 15 min. For the PbI₂ layer, 645.4 mg of PbI₂ was dissolved in the mixed solution of DMF and DMSO (95:5 volume/volume) to obtain the precursor solution of PbI₂. The organic salt solution was the solution containing FAI:MAI:PEAI:MACl (50 mg:36 mg:5.66 mg:9 mg) in IPA solution. For device fabrication, the PbI₂ precursor solution was spin-coated on to the ITO pattern at the speed of 1500 rpm for 30 s, and then annealing of 70 °C for 2 min in the glove box. The organic salt solution was spin-coated on the annealed PbI₂ film at the

rate of 2000 rpm for 30 s. Then the film was annealed on a heating plate at 150 °C for 15 min.

Characterizations: The electrical property measurements were performed by using an Agilent B1500A precision meter in the I - V and I - V - t modes. The PL mapping was obtained by using a laser scanning confocal microscope (Witec, alpha 300). The laser excitation wavelength and power were set to 532 nm and 10 μW, respectively. The photocurrent mapping was characterized by an Agilent B1500A precision meter, and the light source was SuperKExtreme, NKT Photonics. The laser excitation wavelength and power were set to 685 nm and 7 nW, respectively. The response speed of the device was obtained from the photocurrent transient recorded by a Keysight DSOX3104T oscilloscope.

Simulation Methodology: The first principles calculations were performed with density functional theory (DFT) as implemented in CP2K/Quickstep package.^[39] The van der Waals interactions were described by the Grimme DFT-D3 approach.^[40] The function of the standard Perdew-Burke-Ernzerhof (PBE) generalized gradient approximation (GGA)^[41] was employed for exchange correction interactions, within the framework of Gaussian and plane wave (GPW) method.^[42] The wavefunctions of the valence electrons were expanded in terms of Gaussian functions with molecularly optimized (MOLOPT) double ζ -polarized basis sets

(m-DZVP),^[43] and core electrons were described with norm-conserving Goedecker–Teter–Hutter (GTH) pseudopotentials.^[44] The energy cutoff for the plane wave was set at 500 Ry. All the atoms were allowed to relax until the force on each atom was less than 0.01 eV Å^{−1}. Based on the optimized geometries, the transition state calculation was carried out with the climbing nudged elastic band (CINEB).^[45] A total of five images were applied between the initial and the final state, and the force threshold was set to 0.05 eV Å^{−1}.

Supporting Information

Supporting Information is available from the Wiley Online Library or from the author.

Acknowledgements

This work was financially supported by the Beijing Natural Science Foundation (Grant Nos. JQ20027 and 4222065), the National Natural Science Foundation of China (Grant Nos. 62034001, 61974008, 52073005, 22033006, and 62005003).

Conflict of Interest

The authors declare no conflict of interest.

Data Availability Statement

The data that support the findings of this study are available from the corresponding author upon reasonable request.

Keywords

ion migration, passivation, perovskites, photodiodes, self-doping

Received: January 21, 2023
Revised: April 1, 2023
Published online: May 28, 2023

- [1] Y. Shao, Y. Yuan, J. Huang, *Nat. Energy* **2016**, *1*, 15001.
- [2] J. A. Christians, P. Schulz, J. S. Tinkham, T. H. Schloemer, S. P. Harvey, B. J. Tremolet De Villers, A. Sellinger, J. J. Berry, J. M. Luther, *Nat. Energy* **2018**, *3*, 68.
- [3] Q. Jiang, Y. Zhao, X. Zhang, X. Yang, Y. Chen, Z. Chu, Q. Ye, X. Li, Z. Yin, J. You, *Nat. Photonics* **2019**, *13*, 460.
- [4] B. R. Sutherland, A. K. Johnston, A. H. Ip, J. Xu, V. Adinolfi, P. Kanjanaboos, E. H. Sargent, *ACS Photonics* **2015**, *2*, 1117.
- [5] P. Lopez-Varo, J. A. Jiménez-Tejada, M. García-Rosell, S. Ravishanker, G. García-Belmonte, J. Bisquert, O. Almora, *Adv. Energy Mater.* **2018**, *8*, 1702772.
- [6] J.-P. Correa-Baena, A. Abate, M. Saliba, W. Tress, T. J. Jacobsson, M. Grätzel, A. Hagfeldt, *Energy Environ. Sci.* **2017**, *10*, 710.
- [7] Y. Yuan, J. Huang, *Acc. Chem. Res.* **2016**, *49*, 286.
- [8] M. C. Yen, C. J. Lee, K. H. Liu, Y. Peng, J. Leng, T. H. Chang, C. C. Chang, K. Tamada, Y. J. Lee, *Nat. Commun.* **2021**, *12*, 4460.
- [9] X. Yang, Z. Xiong, Y. Chen, Y. Ren, L. Zhou, H. Li, Y. Zhou, F. Pan, S. T. Han, *Nano Energy* **2020**, *78*, 105246.
- [10] X. Guan, Y. Wang, C. H. Lin, L. Hu, S. Ge, T. Wan, A. Younis, F. Li, Y. Cui, D. C. Qi, D. Chu, X. D. Chen, T. Wu, *Appl. Phys. Rev.* **2020**, *7*, 031401.
- [11] C. T. Herrera, J. G. Labram, *Appl. Phys. Lett.* **2020**, *117*, 233501.
- [12] X. Han, W. Wu, H. Chen, D. Peng, L. Qiu, P. Yan, C. Pan, *Adv. Funct. Mater.* **2021**, *31*, 2005230.
- [13] M. Hasan, S. Venkatesan, D. Lyashenko, J. D. Slinker, A. Zakhidov, *Anal. Chem.* **2017**, *89*, 9649.
- [14] Y. Song, W. Bi, A. Wang, X. Liu, Y. Kang, Q. Dong, *Nat. Commun.* **2020**, *11*, 274.
- [15] Y. Liu, Q. Dong, Y. Fang, Y. Lin, Y. Deng, J. Huang, *Adv. Funct. Mater.* **2019**, *29*, 1807707.
- [16] S. J. Yang, M. Kim, H. Ko, D. H. Sin, J. H. Sung, J. Mun, J. Rho, M. H. Jo, K. Cho, *Adv. Funct. Mater.* **2018**, *28*, 1804067.
- [17] W. J. Yin, T. Shi, Y. Yan, *Appl. Phys. Lett.* **2014**, *104*, 063903.
- [18] S. T. Birkhold, J. T. Precht, R. Giridharagopal, G. E. Eperon, L. Schmidt-Mende, D. S. Ginger, *J. Phys. Chem. C* **2018**, *122*, 12633.
- [19] D. Pan, Y. Fu, J. Chen, K. J. Czech, J. C. Wright, S. Jin, *Nano Lett.* **2018**, *18*, 1807.
- [20] G. Y. Kim, A. Senocrate, T. Yang, G. Gregori, M. Grätzel, J. Maier, *Nat. Mater.* **2018**, *17*, 445.
- [21] S. Chen, X. Wen, R. Sheng, S. Huang, X. Deng, M. A. Green, A. Ho-Baillie, *ACS Appl. Mater. Interfaces* **2016**, *8*, 5351.
- [22] Y. Rakita, I. Lubomirsky, D. Cahen, *Mater. Horiz.* **2019**, *6*, 1297.
- [23] Y. T. Li, L. Ding, J. Z. Li, J. Kang, D. H. Li, L. Ren, Z. Y. Ju, M. X. Sun, J. Q. Ma, Y. Tian, G. Y. Gou, D. Xie, H. Tian, Y. Yang, L. W. Wang, L. M. Peng, T. L. Ren, *ACS Cent. Sci.* **2019**, *5*, 1857.
- [24] Y. Chen, W. Zhou, X. Chen, X. Zhang, H. Gao, N. A. N. Ouedraogo, Z. Zheng, C. B. Han, Y. Zhang, H. Yan, *Adv. Funct. Mater.* **2022**, *32*, 2108417.
- [25] J. T. Dubose, P. V. Kamat, *J. Am. Chem. Soc.* **2020**, *142*, 5362.
- [26] P. Cui, D. Wei, J. Ji, H. Huang, E. Jia, S. Dou, T. Wang, W. Wang, M. Li, *Nat. Energy* **2019**, *4*, 150.
- [27] Q. Wang, Y. Shao, H. Xie, L. Lyu, X. Liu, Y. Gao, J. Huang, *Appl. Phys. Lett.* **2014**, *105*, 163508.
- [28] T. Leijtens, G. E. Eperon, A. J. Barker, G. Grancini, W. Zhang, J. M. Ball, A. R. S. Kandada, H. J. Snaith, A. Petrozza, *Energy Environ. Sci.* **2016**, *9*, 3472.
- [29] X. Zhang, X. Chen, Y. Chen, N. A. N. Ouedraogo, J. Li, X. Bao, C. B. Han, Y. Shirai, Y. Zhang, H. Yan, *Nanoscale Adv.* **2021**, *3*, 6128.
- [30] X. Zhang, W. Zhou, X. Chen, Y. Chen, X. Li, M. Wang, Y. Zhou, H. Yan, Z. Zheng, Y. Zhang, *Adv. Energy Mater.* **2022**, *12*, 2201105.
- [31] Y. Lin, Y. Bai, Y. Fang, Z. Chen, S. Yang, X. Zheng, S. Tang, Y. Liu, J. Zhao, J. Huang, *J. Phys. Chem. Lett.* **2018**, *9*, 654.
- [32] L. Li, S. Ye, J. Qu, F. Zhou, J. Song, G. Shen, *Small* **2021**, *17*, 2005606.
- [33] X. Zou, Y. Li, G. Tang, P. You, F. Yan, *Small* **2019**, *15*, 1901004.
- [34] X. Chen, Y. Shirai, M. Yanagida, K. Miyano, *J. Phys. Chem. C* **2019**, *123*, 3968.
- [35] Z. Xiao, Y. Yuan, Y. Shao, Q. Wang, Q. Dong, C. Bi, P. Sharma, A. Gruverman, J. Huang, *Nat. Mater.* **2015**, *14*, 193.
- [36] Z. Ni, H. Jiao, C. Fei, H. Gu, S. Xu, Z. Yu, G. Yang, Y. Deng, Q. Jiang, Y. Liu, Y. Yan, J. Huang, *Nat. Energy* **2022**, *7*, 65.
- [37] Q. Ou, Y. Zhang, Z. Wang, J. A. Yuwono, R. Wang, Z. Dai, W. Li, C. Zheng, Z. Q. Xu, X. Qi, S. Duhm, N. V. Medhekar, H. Zhang, Q. Bao, *Adv. Mater.* **2018**, *30*, 1705792.
- [38] P. Calado, A. M. Telford, D. Bryant, X. Li, J. Nelson, B. C. O'Regan, P. R. F. Barnes, *Nat. Commun.* **2016**, *7*, 13831.
- [39] J. Vandevondele, M. Krack, F. Mohamed, M. Parrinello, T. Chassaing, J. Hutter, *Comput. Phys. Commun.* **2005**, *167*, 103.
- [40] S. Grimme, *J. Comput. Chem.* **2006**, *27*, 1787.
- [41] J. P. Perdew, K. Burke, M. Ernzerhof, *Phys. Rev. Lett.* **1996**, *77*, 3865.
- [42] G. Lippert, J. Hutter, M. Parrinello, *Mol. Phys.* **1997**, *92*, 477.
- [43] J. Vandevondele, J. Hutter, *J. Chem. Phys.* **2007**, *127*, 114105.
- [44] S. Goedecker, M. Teter, *Phys. Rev. B: Condens. Matter Mater. Phys.* **1996**, *54*, 1703.
- [45] G. Henkelman, B. P. Uberuaga, H. Jónsson, *J. Chem. Phys.* **2000**, *113*, 9901.